

Observation of Fermi acceleration with cold atoms

G. Barontini,^{1,*} V. Naniyil,¹ J. P. Stinton,¹ D. Reid,¹ J. M. F. Gunn,¹
H. M. Price,¹ A. B. Deb,¹ D. Caprioli,² and V. Guarrera¹

¹*School Of Physics and Astronomy, University of Birmingham, Edgbaston, Birmingham, B15 2TT, UK.*

²*Department of Astronomy and Astrophysics & E. Fermi Institute,
The University of Chicago, 5640 S Ellis Ave, Chicago, IL 60637, USA.*

(Dated: March 13, 2025)

Cosmic rays are deemed to be generated by a process known as “Fermi acceleration”, in which charged particles scatter against magnetic fluctuations in astrophysical plasmas. The process itself is however universal, has both classical and quantum formulations, and is at the basis of dynamical systems with interesting mathematical properties, such as the celebrated Fermi-Ulam model. Despite its effectiveness in accelerating particles, Fermi acceleration has so far eluded unambiguous verifications in laboratory settings. Here, we realize the first fully controllable Fermi accelerator by colliding ultracold atoms against engineered movable potential barriers. We demonstrate that our Fermi accelerator, which is only 100 μm in size, can produce ultracold atomic jets with velocities above half a meter per second. Adding dissipation, we also experimentally test Bell’s general argument for the ensuing energy spectra, which is at the basis of any model of cosmic ray acceleration. On the one hand, our work effectively opens the window to the study of high energy astrophysics with cold atoms, offering new capabilities for the understanding of phenomena such as diffusive acceleration at collisionless shocks. On the other, the performance of our Fermi accelerator is competitive with those of best-in-class accelerating methods used in quantum technology and quantum colliders, but with substantially simpler implementation and virtually no upper limit.

Particle acceleration plays a central role in modern physics, for example in the high-energy colliders that have unlocked our understanding of the nuclear and sub-nuclear world, in the stability of fusion plasmas, and in the origin of extraterrestrial energetic particles. The energization of charged particles generally involves electromagnetic fields, with the accelerated particles revealing themselves through the non-thermal light that they emit, such as synchrotron radiation and inverse-Compton scattering. In astrophysical settings the energizing electromagnetic fields are typically of motional nature, given the impossibility of sustaining large-scale potential drops in tenuous plasmas. The prototypical example of extraterrestrial energetic particles is the cosmic ray radiation [1, 2]: ultra-relativistic ions and electrons produced in cosmic explosions and compact stellar remnants (novae, supernovae, pulsars, gamma-ray bursts), and relativistic jets launched by black holes (microquasars, active galactic nuclei).

The cornerstone mechanism for the origin of cosmic rays was proposed by E. Fermi [3, 4]: when a particle undergoes a head-on (tail-on) elastic collision with a moving magnetic mirror it gains (loses) kinetic energy, but since head-on encounters are more likely than tail-on ones (think about inverse-Compton scattering), on average the particle’s energy must increase with time. While in astrophysical plasmas this *Fermi acceleration* is realized by scattering charged particles against magnetic fluctuations, the process itself is relevant for a wide range of terrestrial classical [5–7] and quantum [8–10] systems, and has inspired several mathematical models with unique properties [11–13]. In the past two decades, kinetic simulations of astrophysical plasmas exploiting the growing

power of modern supercomputers for solving Maxwell’s equations coupled with a phase-space description of particles, have been able to shed light on how acceleration may occur in astrophysical shocks [14–18], in magnetic reconnection [19–21], and in turbulence [22–24]. Experimentally, several impressive endeavors are working towards producing particle acceleration at shock in laboratory settings [25–29]. However, to date only hints of deviations from thermal distributions have been reported. In fact, sustaining a plasma laser experiment for many acceleration cycles to detect extended spectra of accelerated particles is still out of reach.

In this work we realize a table-top Fermi accelerator in which neutral particles are accelerated with controlled potential mirrors. The basic principle in one dimension (\hat{x}) is shown in Fig. 1a), where we consider a particle initially at rest being scattered between two potential barriers of height A and $A_0 \geq A$. If the barrier A (left in the figure) moves with velocity v_i and if the collision is elastic in the barrier frame, after the collision the particle acquires a velocity $+2v_i$ in the laboratory frame. The collision with the barrier A_0 , instead, simply reverses its motion $v \rightarrow -2v_i$. While traveling back, the particle is hit a second time by the moving barrier, increasing again its velocity by $2v_i$. The process repeats with the frequency of collisions rapidly increasing due to the increasing particle velocity and the decreasing distance between the barriers. When the kinetic energy of the particle $E_k = mv^2/2 = m(2nv_i)^2/2$, with m the mass of the particle and n the number of collisions with the moving barrier, exceeds A , the particle leaves the accelerator. The net result is an acceleration of the particle to a final velocity of $-2nv_i$.

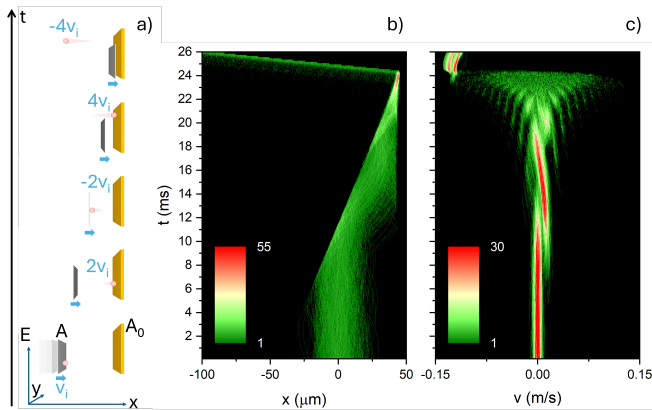


FIG. 1. (a) A particle is hit multiple times by a potential barrier with height A and moving with velocity v_i along the \hat{x} direction, and a stationary potential barrier with height $A_0 \geq A$. Each collision with the moving barrier increases the particle's velocity by $2v_i$. When the kinetic energy of the particle is higher than A , the particle escapes the accelerator. (b) Numerically simulated time evolution of the density distribution along \hat{x} of a cloud of 10^3 non-interacting ^{87}Rb atoms with $T = 50$ nK, inside a Fermi accelerator with $A/k_B = 0.7A_0/k_B = 50$ μK and $v_i = 3.64$ mm/s [30]. The atoms are also subject to a harmonic potential with 40 Hz trapping frequency [30]. The color scale indicates the density in 10^7m^{-3} . The stationary barrier is placed at $x = 45$ μm , while the moving barrier starts at $x = -45$ μm . The two barriers collide for $t = 25$ ms. (c) The same as panel (b) but in the velocity space. The color scale indicates the density in $2 \times 10^4 (\text{m/s})^{-1}$.

As shown in Fig. 1b), the same mechanism holds also for a cloud of trapped ultracold atoms that are initially distributed in real and momentum space according to their temperature. The atomic cloud is compressed in between the two colliding barriers and, in absence of interactions, each atom undergoes the Fermi acceleration process, resulting in an atomic jet exiting the accelerator. The dynamics inside the accelerator can be better appreciated by looking at the characteristic fractal-like evolution in the velocity (or momentum) space, shown in Fig. 1c). Each collision with the barriers adds a 'fringe' to the velocity distribution, increasingly broadening it. As the barriers come close together, the rate of collisions with the barriers drastically increases, and with it the broadening of the velocity distribution. This process continues until the threshold $v = \sqrt{2A/m}$ is reached and the atoms can leave the accelerator. Because this accelerator is based on a threshold process, the width of the distribution of the ejected atoms is essentially dictated by the width of the distribution at $t = 0$ [30].

Our Fermi accelerator is implemented with ultracold ^{87}Rb atoms and potential barriers generated by laser light. The barriers are dynamically shaped with a digital micromirror device [30], and their height is controlled with the power and detuning of the laser beam [30].

The atoms are initially trapped in a crossed beam dipole trap, which is deformed into a one dimensional waveguide along the direction of the accelerator before the acceleration process begins. This is done to support the atomic jet against gravity [30]. In Fig. 2a) we report a typical experimental sequence for an accelerator with $A/k_B = 0.7A_0/k_B \simeq 170$ μK , where k_B is the Boltzmann constant, observed with absorption imaging. The moving barrier, whose position is approximately indicated by the black dashed line, hits the ultracold sample that is initially at rest. The center of mass of the atomic cloud then moves with velocity $2v_i$ towards the static barrier, indicated by the yellow dashed line. Similarly to Fig. 1b), the subsequent microscopic dynamics cannot be resolved in situ, due to the spread of the cloud in momentum and real space. Nonetheless, the net effect of the Fermi acceleration acting on all the atoms manifests itself with the atoms being ejected from the accelerator. As a result of the acceleration process, we observe atomic jets traveling at high speed in the waveguide, as shown in Fig. 1c).

In our experiment, we can observe the full evolution in momentum space by utilizing barriers with relatively low values of A . As an example, in Fig. 2c) we report the measured density distribution along x after 22 ms of time-of-flight, for an accelerator that has a rather low moving barrier with $A/k_B \simeq 1.8$ μK . We can clearly observe two collisions with the moving barrier (the two fringes on the right) and two with the stationary barrier (fringes on the left). After the second collision with the fixed barrier, the atoms have sufficient energy to fly over the moving barrier and exit the accelerator. In Fig. 2d) we report the evolution according to our numerical simulations for the same parameters as Fig. 2c) [30], finding remarkable agreement. Fig. 2e) displays the corresponding density distribution in the velocity space that, as expected, mirrors what is observed in time-of-flight. Note the spreading of the momentum distribution while the atoms are inside the accelerator, and the narrow momentum distribution of the atomic jet. For larger values of A , the observation of the full evolution of the density distribution in momentum space becomes challenging. In fact, as the spread in velocity increases, we cannot use standard time-of-flight methods, since most of the atoms rapidly fly out of our field of view.

We infer the velocity of the atomic jet by measuring the position of its center of mass as a function of time [30]. The results for a wide range of values of A are reported in Fig. 3a). By controlling A over two orders of magnitude, we can finely control the speed of the atomic jet. Note that, despite the fact that the maximum speed of our barrier is limited to 22 mm/s [30], we are able to accelerate our ultracold cloud up to more than 0.5 m/s in 5 ms. This is competitive with what is obtained in free-fall with sequential Bragg large momentum transfer techniques [31] and Bloch oscillations in an optical lattice [32], and more effective than other in-trap techniques

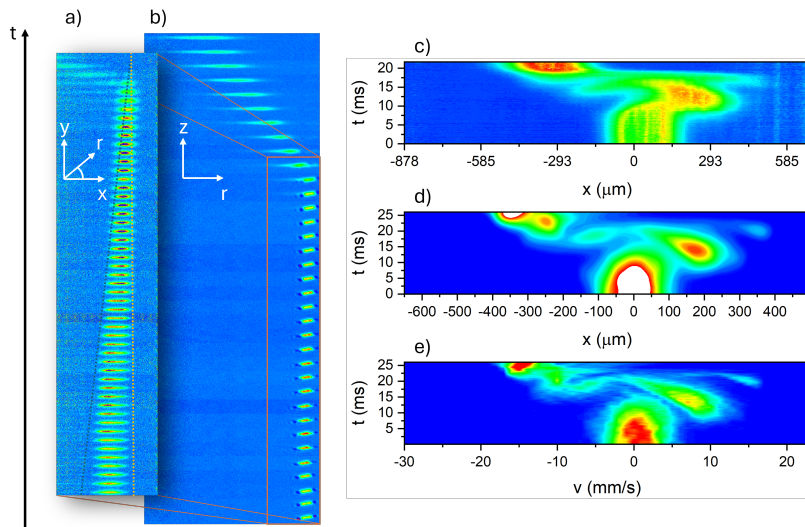


FIG. 2. (a) Stacked in situ absorption images of the atomic cloud taken along \hat{z} . Snapshots are taken every 0.5 ms, the total time is 25.5 ms. Each snapshot is $243 \mu\text{m}$ along \hat{x} and $64.5 \mu\text{m}$ along \hat{y} . The black and yellow dashed lines approximately indicate the position of the moving and stationary barrier respectively. At $t = 0$ there are $\simeq 25 \times 10^3$ atoms at $\simeq 20$ nK. The moving barrier has a speed of 3.6 mm/s, and $A/k_B = 0.7A_0/k_B = 170 \mu\text{K}$. (b) Stacked in situ absorption images of the atomic cloud taken along a direction that is tilted by 50 degrees with respect to \hat{x} . The experimental parameters are the same as in panel (a), but this imaging features lower resolution and larger field of view. Snapshots are taken every ms, the total time is 37 ms. Each snapshot is $1093 \mu\text{m}$ along \hat{x} and $132 \mu\text{m}$ along \hat{z} . (c) The contour plot is the result of 250 stacked absorption images taken along the same direction as panel (b), and integrated along \hat{z} . Each absorption image has been taken after 22 ms of ‘time of flight’ inside the waveguide oriented along \hat{x} . The horizontal scale has been rescaled to account for the 50 degrees angle between the imaging direction and \hat{x} . Note that the images at low t are heavily saturated. The parameters for the Fermi accelerator are $A/k_B = 0.7A_0/k_B = 1.8 \mu\text{K}$ and $v_i = 3.6$ mm/s. (d) Density distribution resulting from the numerical simulations with the same parameters of the experiment shown in (c) [30]. The color scale has been saturated to mimic the experiment. (e) Density distribution in velocity (momentum) space inside the accelerator for the simulations in (d).

based, for example, on magnetic time-averaged adiabatic potentials [33]. As discussed in [30], the maximum velocity achievable in our experiment is limited only by atom losses caused by the use of near-resonant light for the generation of the optical potentials. There are however no fundamental limitations to the maximum velocity achievable, if dissipation is minimized [30]. In Fig. 3b) we report the calculated kinetic energy for the data of Fig. 3a), where it is apparent that $E_k \simeq A$ independently on the shape and velocity of the barriers, and the temperature of the atoms (see also [30]).

From Fig. 2b) one can observe that the width of the accelerated cloud increases as the atoms propagate in the waveguide. The speed at which the atomic jet spreads is given by the width of the distribution in momentum space, and it can be linked to an ‘effective temperature’ [30]. The comparison of our data with a simple numerical model shows that the effective temperature in our experiment, which is typically between 1 and 10 μK depending on the details of the accelerator [30], is mainly determined by atom-atom collisions during the acceleration [30]. In fact, as the barriers approach each other the density of the sample and the average velocity greatly increase, leading to a boost of the atom-atom collisional rate. Such collisions redistribute part of the gained ki-

netic energy in the perpendicular directions, and lead to a ‘dephasing’ of the Fermi mechanism. Remarkably, we have found however that our Fermi accelerator is robust against interactions, as they have no impact on the velocity of the atomic jet (Fig. 3) [30], and their effect on the effective temperature can be drastically reduced or controlled by engineering the shape of the barriers [30].

We finally utilize our setup to experimentally test the famous Bell’s argument [34], which is one of the cornerstones of modern high-energy astrophysics, where extended power-law distributions are routinely observed, both in the cosmic radiation (electrons, nuclei, and neutrinos) and in the non-thermal emission from astrophysical objects. Bell argued that power-law distributions generally arise as the result of a combination of energy gain and particle escape from the accelerator. In our system, Bell’s argument predicts that the energy spectrum inside the accelerator must have the form $N_n = N_1(E_n/E_1)^{-Q}$ with $Q = -\ln(P)/\ln(G)$, where $N_1(E_1)$ and $N_n(E_n)$ are the number of atoms (average energy) after one and n collisions with the moving barrier respectively. P and G are the survival probability and energy gain after each collision [30]. To verify this prediction, we slightly modified the experimental sequence so to measure the number of atoms left and their average velocity after each colli-

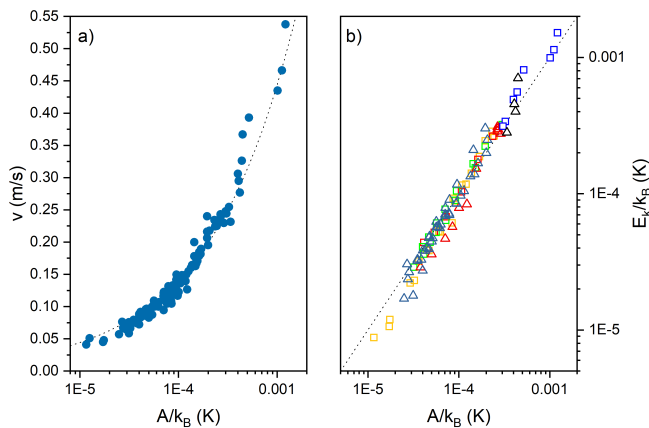


FIG. 3. (a) Measured velocity of the atoms escaping the accelerator as a function of the height of the moving barrier A . The dotted line corresponds to $\sqrt{2A/m}$. (b) Kinetic energy of the particles exiting the accelerator for the data points reported in panel (a). Square symbols are for flat moving potential barriers, triangular symbols are for convex triangular moving barriers [30]. The parameters for the yellow squares are $v_i = 11$ mm/s and $T=200$ nK, blue squares $v_i = 22$ mm/s and $T=200$ nK, red squares $v_i = 5.5$ mm/s and $T=20$ nK, green squares $v_i = 4.4$ mm/s and $T=20$ nK. The parameters for the red triangles are $v_i = 5.5$ mm/s and $T=20$ nK, black triangles $v_i = 5.5$ mm/s and $T=250$ nK, blue triangles $v_i = 4.4$ mm/s and $T=20$ nK [30]. Note that for the right-most points the acceleration experienced by the atoms is $\simeq 10$ times the gravitational acceleration. The dashed line is the bisector. The vertical errorbars are smaller than the size of the data points in both panels. The values of A have a 5% systematic uncertainty (not shown) coming from slow drifts in the focussing of the barriers.

sion with the barriers [30]. By controlling the detuning and power of the laser light that generates the potential barriers, we are able to tune the light-atom scattering rate Γ_s , which in turn determines P , leaving all the other parameters of the experiment unchanged. In Fig. 4a) we report our results on the number of atoms left in the accelerators as a function of their average energy, for different values of Γ_s . Our data are well fitted by the power-law function described above (solid lines), with $Q = -\Theta/\ln(G)$, where Θ is the fitting parameter and G is a function of E_n/E_1 [30]. In general, atom losses in our system are a combination of losses coming from the light-atom scattering discussed above and other loss mechanisms that don't depend on the detuning, the most relevant being three-body collisions. For this reason, in our experiment we expect the survival probability to have the form $P = (\gamma_0 + \xi\Gamma_s)^{-1}$, where γ_0 accounts for all the detuning-independent loss mechanisms and ξ for the effective interaction time of the atoms with the barriers. As shown in Fig. 4b), the scaling of the Θ parameter observed in our experiment is remarkably compatible with the functional dependence $\Theta = \ln(\gamma_0 + \xi\Gamma_s) \equiv \ln(P)$ (solid line), as predicted by Bell's argument.

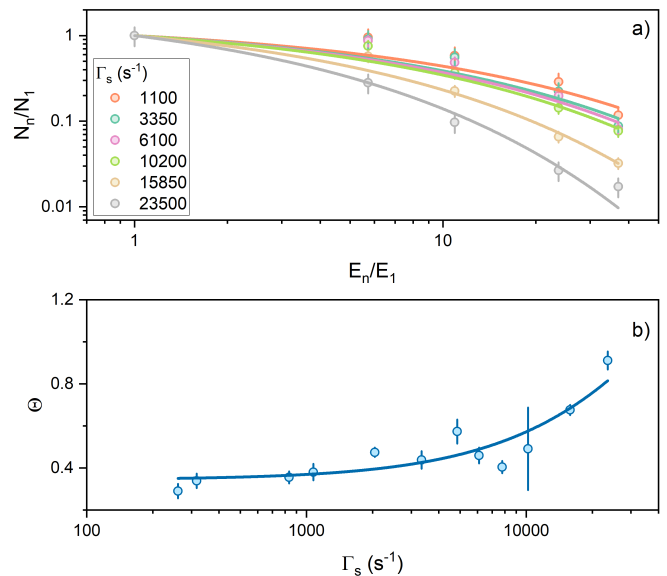


FIG. 4. (a) The solid symbols are the number of atoms remaining inside the accelerator as a function of their average kinetic energy, for different values of the light-atom scattering rate. Each data point is taken after a collision with the moving barrier. Both the number of atoms and the energy are normalized with respect to the figures we obtain after the first collision with the barriers [30]. The errorbars are 1σ statistical errors. The solid lines are fits to the data with a power-law function [30]. (b) Data points are the value of the exponent Θ obtained by the fits in panel (a) and additional data shown in [30], as a function of the calculated scattering rate stemming from the potential barriers. The errorbars come from the fitting procedure. The solid line is a fit to the data with the function $\Theta = \ln(\gamma_0 + \xi\Gamma_s)$, with $\gamma_0 = (2.1 \pm 0.2)$ and $\xi = (1.1 \pm 0.2) \times 10^{-4}$ s.

Our results show that cold atom technology is an ideal platform to implement and study Fermi acceleration processes and related phenomena. For example it can be used as a testbed for classical, dissipative and quantum Fermi-Ulam models [8, 11–13], and can provide new opportunities towards the understanding of complex mechanisms such as diffusive shock acceleration in astrophysical plasmas [34–38]. In this direction, particularly appealing is the ability of cold atom experiments to engineer the interactions between the atoms [39, 40]. Our methods can for example be straightforwardly applied to ultracold neutral plasmas [41, 42], where some of the conditions found in astrophysical settings could be obtained [43]. In the context of quantum technology, our Fermi accelerator enables to obtain samples with large E_k and low effective temperatures, that are desirable features in quantum chemistry [44–46] and quantum colliders applications [47–49]. With respect to other record-achieving techniques in atom optics [50], a Fermi accelerator is characterized by a remarkably simple implementation, which makes it ideally suited for in-trap atomtronics applications [51]. Fermi acceleration can be also

used to direct and split atomic samples into two counter-propagating clouds [30], thus providing complementary features to existing techniques [31, 32]. Finally, the study of quantum Fermi acceleration [8, 30] could be a promising avenue for quantum information science, as there is concrete potential for the development of new tools for the manipulation of quantum wavepackets .

Acknowledgments: We acknowledge fruitful discussion with the cold atoms group and the theoretical physics group at the University of Birmingham, and the use of computing power provided by the Advanced Research Computing centre at the University of Birmingham. This work was supported by EP-SRC through grants EP/V027948/1, EP/R021236/1, 2740639 and EP/W016141/1, by NASA through grants 80NSSC18K1218, NSSC23K0088, and 80NSSC24K0173, by NSF through grants PHY-2010240 and AST-2009326, and by the Royal Society through grants UF160112, RGF/EA/180121 and RGF/R1/180071.

* g.barontini@bham.ac.uk

- [1] M. S. Longair, *High Energy Astrophysics*, 3rd ed. (Cambridge University Press, 2011).
- [2] T. K. Gaisser, R. Engel, and E. Resconi, *Cosmic Rays and Particle Physics* ([Cambridge University Press], 2016).
- [3] E. Fermi, On the Origin of the Cosmic Radiation, *Physical Review* **75**, 1169 (1949).
- [4] E. Fermi, Galactic Magnetic Fields and the Origin of Cosmic Radiation., *Ap. J.* **119**, 1 (1954).
- [5] M. A. Lieberman and V. A. Godyak, From fermi acceleration to collisionless discharge heating, *IEEE transactions on plasma science* **26**, 955 (1998).
- [6] K. Sacha and J. Zakrzewski, Time crystals: a review, *Reports on Progress in Physics* **81**, 016401 (2017).
- [7] A. Steane, P. Szriftgiser, P. Desbiolles, and J. Dalibard, Phase modulation of atomic de broglie waves, *Phys. Rev. Lett.* **74**, 4972 (1995).
- [8] J. V. José and R. Cordery, Study of a quantum fermi-acceleration model, *Phys. Rev. Lett.* **56**, 290 (1986).
- [9] A. Pizzi, J. Knolle, and A. Nunnenkamp, Higher-order and fractional discrete time crystals in clean long-range interacting systems, *Nature communications* **12**, 2341 (2021).
- [10] S. Barbosa, M. Kiefer-Emmanouilidis, F. Lang, J. Koch, and A. Widera, [Stabilizing an ultracold fermi gas against fermi acceleration to superdiffusion through localization](#) (2024), [arXiv:2311.08224 \[cond-mat.quant-gas\]](#).
- [11] S. Ulam, On some statistical properties of dynamical systems, *Proc. 4th Berkeley Symp. on Math. Stat. and Prob.* **3**, 315 (1961).
- [12] A. Brahic, Numerical study of a simple dynamical system. i. the associated plane area-preserving mapping, *Astr. and Astrophys.* **12**, 98 (1971).
- [13] M. A. Lieberman and A. J. Lichtenberg, Stochastic and adiabatic behavior of particles accelerated by periodic forces, *Phys. Rev. A* **5**, 1852 (1972).
- [14] M. A. Malkov and L. O’C. Drury, Nonlinear theory of diffusive acceleration of particles by shock waves, *Rep. Prog. Phys.* **64**, 429 (2001).
- [15] A. Spitkovsky, Particle Acceleration in Relativistic Collisionless Shocks: Fermi Process at Last?, *Astrophysical Journal Letters* **682**, L5 (2008), [arXiv:arXiv:0802.3216](#).
- [16] H. Karimabadi, V. Roytershteyn, H. X. Vu, Y. A. Omelchenko, J. Scudder, W. Daughton, A. Dimmock, K. Nykyri, M. Wan, D. Sibeck, M. Tatineni, A. Majumdar, B. Loring, and B. Geveci, The link between shocks, turbulence, and magnetic reconnection in collisionless plasmas, *Physics of Plasmas* **21**, 062308 (2014).
- [17] D. Caprioli and A. Spitkovsky, Simulations of Ion Acceleration at Non-relativistic Shocks: I. Acceleration Efficiency, *Astrophysical Journal* **783**, 91 (2014), [arXiv:1310.2943 \[astro-ph.HE\]](#).
- [18] D. Caprioli, C. C. Haggerty, and P. Blasi, Kinetic Simulations of Cosmic-Ray-modified Shocks. II. Particle Spectra, *Astrophysical Journal* **905**, 2 (2020), [arXiv:2009.00007 \[astro-ph.HE\]](#).
- [19] L. Sironi and A. Spitkovsky, Particle Acceleration in Relativistic Magnetized Collisionless Electron-Ion Shocks, *Astrophysical Journal* **726**, 75 (2011), [arXiv:1009.0024 \[astro-ph.HE\]](#).
- [20] B. Cerutti, G. R. Werner, D. A. Uzdensky, and M. C. Begelman, Three-dimensional Relativistic Pair Plasma Reconnection with Radiative Feedback in the Crab Nebula, *Astrophysical Journal* **782**, 104 (2014), [arXiv:1311.2605 \[astro-ph.HE\]](#).
- [21] M. Petropoulou, D. Giannios, and L. Sironi, Blazar flares powered by plasmoids in relativistic reconnection, *MNRAS* **462**, 3325 (2016), [arXiv:1606.07447 \[astro-ph.HE\]](#).
- [22] L. Comisso and L. Sironi, Particle Acceleration in Relativistic Plasma Turbulence, *Physical Review Letters* **121**, 255101 (2018), [arXiv:1809.01168 \[astro-ph.HE\]](#).
- [23] F. Pecora, S. Servidio, A. Greco, W. H. Matthaeus, D. Burgess, C. T. Haynes, V. Carbone, and P. Veltri, Ion diffusion and acceleration in plasma turbulence, *Journal of Plasma Physics* **84**, 725840601 (2018), [arXiv:1803.09647 \[physics.plasm-ph\]](#).
- [24] V. Zhdankin, D. A. Uzdensky, G. R. Werner, and M. C. Begelman, Electron and Ion Energization in Relativistic Plasma Turbulence, *Physical Review Letters* **122**, 055101 (2019), [arXiv:1809.01966 \[astro-ph.HE\]](#).
- [25] F. Fiuza, G. Swadling, A. Grassi, H. Rinderknecht, D. Higginson, D. Ryutov, C. Bruulsema, R. Drake, S. Funk, S. Glenzer, *et al.*, Electron acceleration in laboratory-produced turbulent collisionless shocks, *Nature physics* **16**, 916 (2020).
- [26] D. B. Schaeffer, W. Fox, R. K. Follett, G. Fiksel, C. K. Li, J. Matteucci, A. Bhattacharjee, and K. Germaschewski, Direct observations of particle dynamics in magnetized collisionless shock precursors in laser-produced plasmas, *Phys. Rev. Lett.* **122**, 245001 (2019).
- [27] C. K. Li, V. T. Tikhonchuk, Q. Moreno, H. Sio, E. D’Humières, X. Ribeyre, P. Korneev, S. Atzeni, R. Betti, A. Birkel, E. M. Campbell, R. K. Follett, J. A. Frenje, S. X. Hu, M. Koenig, Y. Sakawa, T. C. Sangster, F. H. Seguin, H. Takabe, S. Zhang, and R. D. Petrasso, Collisionless shocks driven by supersonic plasma flows with self-generated magnetic fields, *Phys. Rev. Lett.* **123**, 055002 (2019).
- [28] W. Yao, A. Fazzini, S. Chen, K. Burdonov, P. Antici, J. Béard, S. Bolaños, A. Ciardi, R. Diab, E. Filippov, *et al.*, Laboratory evidence for proton energization by col-

- lisionless shock surfing, *Nature Physics* **17**, 1177 (2021).
- [29] D. Yuan, Z. Lei, H. Wei, Z. Zhang, J. Zhong, Y. Li, Y. Ping, Y. Zhang, Y. Li, F. Wang, *et al.*, Electron stochastic acceleration in laboratory-produced kinetic turbulent plasmas, *Nature Communications* **15**, 5897 (2024).
- [30] See Supplemental Material for details.
- [31] S.-w. Chiow, T. Kovachy, H.-C. Chien, and M. A. Kasevich, $102\hbar k$ large area atom interferometers, *Phys. Rev. Lett.* **107**, 130403 (2011).
- [32] L. Morel, Z. Yao, P. Clade, and S. Guellati-Khelifa, Determination of the fine-structure constant with an accuracy of 81 parts per trillion, *Nature* **588**, 61 (2020).
- [33] S. Pandey, H. Mas, G. Drougakis, P. Thekkepatt, V. Bolpasi, G. Vasilakis, K. Poullos, and W. von Klitzing, Hypersonic bose–einstein condensates in accelerator rings, *Nature* **570**, 205 (2019).
- [34] A. R. Bell, The acceleration of cosmic rays in shock fronts – i, *Monthly Notices of the Royal Astronomical Society* **182**, 147 (1978), <https://academic.oup.com/mnras/article-pdf/182/2/147/3710138/mnras182-0147.pdf>.
- [35] G. Krymskii, A regular mechanism for the acceleration of charged particles on the front of a shock wave, in *Akademiia Nauk SSSR Doklady*, Vol. 234 (1977) pp. 1306–1308.
- [36] W. Axford, E. Leer, and G. Skadron, The acceleration of cosmic rays by shock waves, in *International cosmic ray conference*, Vol. 11 (Springer, 1977).
- [37] R. D. Blandford and J. P. Ostriker, Particle acceleration by astrophysical shocks, *Astrophysical Journal*, Part 2-Letters to the Editor, vol. 221, Apr. 1, 1978, p. L29-L32. **221**, L29 (1978).
- [38] A. Bell, The acceleration of cosmic rays in shock fronts–ii, *Monthly Notices of the Royal Astronomical Society* **182**, 443 (1978).
- [39] C. Chin, R. Grimm, P. Julienne, and E. Tiesinga, Feshbach resonances in ultracold gases, *Rev. Mod. Phys.* **82**, 1225 (2010).
- [40] M. Deiss, S. Willitsch, and J. Hecker Denschlag, Cold trapped molecular ions and hybrid platforms for ions and neutral particles, *Nature Physics* **20**, 713–721 (2024).
- [41] T. K. Langin, G. M. Gorman, and T. C. Killian, Laser cooling of ions in a neutral plasma, *Science* **363**, 61 (2019).
- [42] T. Kroker, M. Grossman, K. Sengstock, M. Drescher, P. Wessels-Staarmann, and J. Simonet, Ultrafast electron cooling in an expanding ultracold plasma, *Nature Communications* **12**, 529 (2021).
- [43] S. Ichimaru, Strongly coupled plasmas: high-density classical plasmas and degenerate electron liquids, *Rev. Mod. Phys.* **54**, 1017 (1982).
- [44] B. R. Heazlewood and T. P. Softley, Towards chemistry at absolute zero, *Nat Rev Chem* **5**, 125 (2021).
- [45] S. Ospelkaus, K.-K. Ni, D. Wang, M. De Miranda, B. Neyenhuis, G. Quéméner, P. Julienne, J. Bohn, D. Jin, and J. Ye, Quantum-state controlled chemical reactions of ultracold potassium-rubidium molecules, *Science* **327**, 853 (2010).
- [46] A. Henson, S. Gersten, Y. Shagam, J. Narevicius, and E. Narevicius, Observation of resonances in penning ionization reactions at sub-kelvin temperatures in merged beams, *Science* **338**, 234 (2012).
- [47] K. Gibble, S. Chang, and R. Legere, Direct observation of *s*-wave atomic collisions, *Phys. Rev. Lett.* **75**, 2666 (1995).
- [48] R. A. Hart, X. Xu, R. Legere, and K. Gibble, A quantum scattering interferometer, *Nature* **446**, 892 (2007).
- [49] T. Ryan, K. O. Roberts, E. Tiesinga, A. C. Wade, B. Blakie, A. B. Deb, and N. Kjærgaard, Multiple scattering dynamics of fermions at an isolated p-wave resonance, *Nature Communications* **7**, 12069 (2016).
- [50] G. D. McDonald, C. C. N. Kuhn, S. Bennetts, J. E. Debs, K. S. Hardman, M. Johnsson, J. D. Close, and N. P. Robins, $80\hbar k$ momentum separation with bloch oscillations in an optically guided atom interferometer, *Phys. Rev. A* **88**, 053620 (2013).
- [51] L. Amico, D. Anderson, M. Boshier, J.-P. Brantut, L.-C. Kwek, A. Minguzzi, and W. von Klitzing, Colloquium: Atomtronic circuits: From many-body physics to quantum technologies, *Rev. Mod. Phys.* **94**, 041001 (2022).
- [52] A. Smith, T. Easton, V. Guarrera, and G. Barontini, Generation of optical potentials for ultracold atoms using a superluminescent diode, *Phys. Rev. Res.* **3**, 033241 (2021).
- [53] C. Oliver, A. Smith, T. Easton, G. Salerno, V. Guarrera, N. Goldman, G. Barontini, and H. M. Price, Bloch oscillations along a synthetic dimension of atomic trap states, *Phys. Rev. Res.* **5**, 033001 (2023).

SUPPLEMENTARY MATERIALS

Experimental sequences

Details of our experimental apparatus and our typical experimental sequence are provided in [52, 53] and references therein. In brief, we prepare ultracold clouds of ^{87}Rb by forced evaporative cooling in a crossed beam dipole trap. Unless differently specified, the atoms are initially trapped in a harmonic trap with frequencies $(\omega_x, \omega_y, \omega_z) = 2\pi \times (37, 70, 70)$ Hz and have an initial temperature of $\simeq 20$ nK. Once the acceleration process begins, the trapping potential is deformed in 100 ms into a one dimensional waveguide oriented along the direction of the accelerator. This is done by linearly ramping up the power of one of the trapping beams and switching off the other. The trapping frequencies at the end of the transformation are $(\omega_x, \omega_y, \omega_z) = 2\pi \times (40, 800, 800)$ Hz. We do not observe any appreciable loss of atoms in the process. At this stage, and without leaving the atoms the time to thermalize, we switch on the barriers and trigger the motion of the moving one. Note that the potential along \hat{x} is harmonic only close to the waist of the trapping beam, where the atoms are initially. The actual shape of the potential has the typical Gaussian behavior, that becomes almost flat after $\simeq 150 \mu\text{m}$.

At the beginning of our typical sequence our sample features a large condensed fraction. However, as soon as the cloud is hit by the moving barrier, the condensate fraction vanishes. This is expected because, for almost all our data, the barrier moves faster than the speed of sound in the condensate (see also below). We have additionally verified that there are no measurable differences in the properties of the atomic jet when starting with a condensed or non-condensed cloud. For these reasons - and for simplicity- the whole discussion in the main text as well as the numerical simulations consider our sample to be an ultracold thermal gas rather than a quantum gas already from $t = 0$.

The shaped light used to generate the potential barriers is shone on the sample from the \hat{z} direction [52, 53]. The atoms are measured by absorption imaging along the same direction utilizing an optical system with $20\times$ magnification. Typical absorption images are shown in Fig. 2a). We also image the atoms with a $2.6\times$ magnification optical system from a direction perpendicular to \hat{z} and tilted by 50 degrees with respect to the direction of motion of the moving barrier, i.e., \hat{x} . Typical images taken from this direction are shown in Fig. 2b) and c), and and Fig. S6b). We mostly utilize this imaging direction for the quantitative analysis of the atomic jet properties.

To measure the properties of the atomic jets we perform two dimensional fits of the absorption images. The typical shape of the atomic jet along \hat{x} is close to an asymmetric Gaussian [see Fig. 2b) and S3c)]. We found

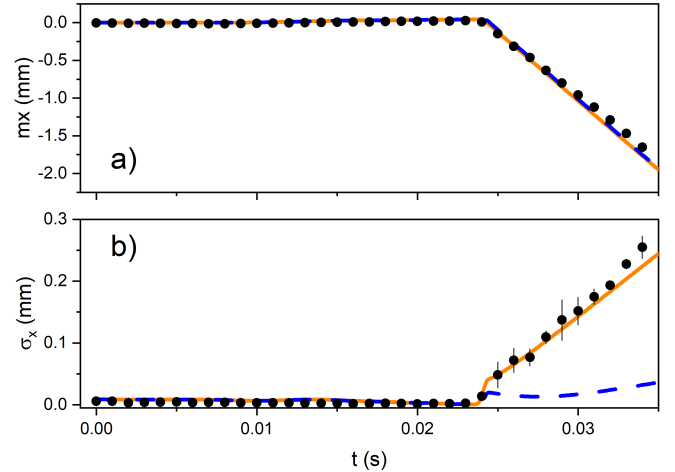


FIG. S1. (a) The solid symbols are the measured center of mass of the atomic cloud along x as a function of time for an atomic cloud of $\simeq 25 \times 10^3$ atoms with $T \simeq 20$ nK at $t = 0$. The accelerator features $A = 0.7A_0 = 170 \mu\text{K}$ and $v_i = 3.64$ mm/s. The measured values are rescaled accounting for the 50 degrees angle between the imaging direction and the x axis. The dashed blue (solid orange) line is the result of the numerical simulations without (with) interactions. The errorbars, which are 1σ statistical errors, are smaller than the size of the points. (b) The solid symbols are the measured widths of the atomic cloud along x as a function of time. The measured values are rescaled accounting for the 50 degrees angle between the imaging direction and the x axis. The dashed blue (solid orange) line is the result of the numerical simulations without (with) interactions. The errorbars are 1σ statistical errors.

however that fitting our data with a symmetric Gaussian delivers the same results than using an asymmetric one (with a small offset for the width). For simplicity we have therefore utilized a symmetric Gaussian function to fit the majority of our data, extracting the position m_r and width σ_r of the atomic jet along \hat{r} . We then rescale these values to account for the angle between the imaging direction and the x propagation axis, obtaining m_x and σ_x . The typical results for an experimental sequence like the one shown in Fig. 2b) is reported in Fig. S1. Once the atomic jet leaves the accelerator, we extract its velocity from the slope of the curve m_x vs. t (shown in Fig. 3), and its effective temperature (see below) from the slope of the curve σ_x vs. t .

Generation of dynamical potentials with the DMD

The DMD is a 1920×1080 matrix of micromirrors that can be independently controlled [52, 53]. Each micromirror can only be turned on or off, therefore to obtain an effective ‘grey scale’ we utilize image dithering methods (either ordered dithering by tiling a Bayer matrix or Floyd-Steinberg dithering). These create patterns of black and

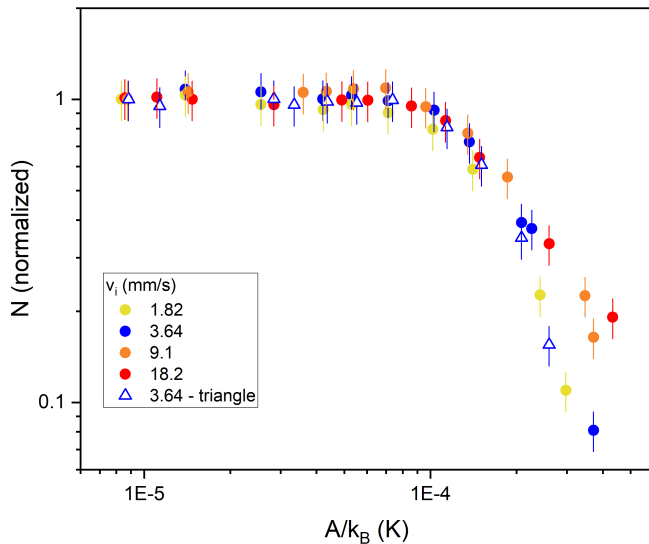


FIG. S2. Normalized number of atoms as a function of the height of the moving barrier, for different velocities and shapes of the moving barrier. In this measurement the power of the laser was kept constant at $\simeq 5.2$ mW, and A was controlled with the detuning with respect to the atomic transition. The errorbars are 1σ statistical errors.

white pixels so that when they are averaged over an area, they approximate the wanted grey-scale value. We utilize this feature to control the A/A_0 ratio. Typically we set the fixed barrier to be ‘fully on’, and we set the relative height of the moving barrier by using the grey scale. For the vast majority of our measurements, we set the width of the (flat) moving barrier to be $5\ \mu\text{m}$, and the one of the fixed barrier to be $20\ \mu\text{m}$. The optical resolution of our system is $\simeq 1\ \mu\text{m}$, setting a limit to the steepness of our barriers. We have tested barriers with different widths, steepness and with different steepness functions, finding no appreciable differences between them over the range of parameters explored.

To realize moving barriers, we upload on the DMD a sequence of images where the barrier is increasingly displaced, and then we refresh the DMD pattern with a rate controlled by a TTL generator. The travel distance is usually $91\ \mu\text{m}$, with the initial and final position of the moving barrier (this latter coinciding with the position of the fixed barrier) equally distant from the atomic cloud at $t = 0$. To control v_i , we can either change the number of images needed for the barrier to move from the initial to the final position, and/or the refresh rate of the DMD.

The optical dipole potential is generated using a Ti:Sa laser tuned near the D2 transition of ^{87}Rb . The Ti:Sa outputs approximately 800 mW. After passing through an AOM, an optical fiber, and the dedicated optical setup [52] (with the DMD fully ‘on’), we measure $\simeq 7 \pm 1$ mW of light on the atoms, depending on the detuning. The main bottleneck in the system is the reflectance of the DMD, which is only 10%, far less than the expected 50%, ac-

ording to the specifications of the device. Since the laser power at our disposal is rather limited and $A \propto 1/\Delta$, with Δ the laser detuning, to reach large values of A it is necessary to reduce Δ . However, the photon scattering rate Γ_s scales as $1/\Delta^2$, substantially increasing atom losses for larger values of A . We use this feature for the measurements reported in Fig. 4. While the use of non-conservative potentials is crucial in our experiment for the verification of Bell’s argument, higher powers would enable us to reach higher values of A with larger values of Δ , therefore reducing Γ_s .

For this work the laser is tuned between $\simeq 779.5$ and $\simeq 780.23$ nm resulting in blue detunings between $\simeq 450$ and $\simeq 25$ GHz. In Fig. S2 we report the dependence of the number of atoms in the atomic jet as a function of A (and therefore as a function of $1/\Delta$). This shows that the reduced power at our disposal is the main limitation to reach larger values of A . For the highest values of A that we can reach, atom losses can be slightly reduced with higher barrier velocities, that reduce the number of collisions needed for an atom to escape the accelerator. However, due to technical reasons (see below) our Fermi accelerator delivers better performance with low barrier velocities. Note that triangular shaped barriers (see below) feature higher loss rates than flat barriers because they have a larger area. As discussed earlier, with more power at our disposal it would be possible to achieve better performance in terms of acceleration. Indeed, there are in principle no limitations to the maximum velocity achievable if dissipation is minimized (see below).

Effective temperature

For a gas in equilibrium, the temperature determines the speed of the spreading of the sample in time of flight. Since the atomic jet is not in thermal equilibrium, we associate its spreading, i.e. the increasing of σ_x in time [as shown in Fig. S1b)], to an ‘effective temperature’ T^* . When using flat barriers as those depicted in Fig. 1, the values of T^* observed in the experiment are at least one order of magnitude lower than E_k . By comparing the data with the numerical model described below, we conclude that T^* is mainly determined by atom-atom collisions during the acceleration. In Fig. S6 we report the measured ratio T^*/E_k for the data of Fig. 3, around $A \simeq 100\ \mu\text{K}$. We observe that the effect of the interactions on T^* can be substantially reduced by engineering the shape of the barriers (red triangles in Fig. S6). Our model shows that for non-interacting atoms, and considering all experimental imperfections, it could be possible to reach $T^*/E_k \leq 10^{-3} - 10^{-5}$ with the same parameters as our experiment.

Numerical simulations

For Fig. 1b) and c) we simulate our experiment using a molecular dynamics Runge-Kutta algorithm for 1000 atoms with a time resolution of $1 \mu\text{s}$. The simulations do not include atom-atom interactions and enable us to account for several experimental imperfections including the resolution of the optical system ($\simeq 1 \mu\text{m}$), that results in barriers having a finite sharpness, and tilting between the axis of the trap and the motion of the barriers. In the simulations we utilize realistic trapping potentials resulting from the crossing of two Gaussian beams, in accordance with our experimental setup [52, 53].

We utilize this algorithm to simulate a Fermi accelerator with the same parameters as the data sets in Fig. 2 a) and b). The corresponding evolution of the density distribution in real and velocity (momentum) space (both along x) is reported in S3 A and B respectively. The evolution in real space qualitatively coincides with what is observed experimentally. As also discussed in the main text, the evolution in momentum space is rather peculiar to the Fermi acceleration. It is possible to observe the subsequent and more frequent collisions with the barriers that spread the momentum distribution while the atoms are inside the accelerator. Because the Fermi acceleration is a ‘threshold’ process, and in this case the threshold is lower on the side of negative momenta ($A \leq A_0$), the width of the distribution of the expelled atom returns to be rather narrow, and similar to the width of the distribution at $t = 0$. Our simulations predict $T^* \simeq 200 \text{ nK}$, mostly due to the radial compression from the crossed trap to the waveguide.

The dashed lines in Fig. S1 are the evolution of the center of mass and RMS size of the atomic cloud as a function of time for the same set of simulations. While the agreement concerning the velocity of the atomic jet is very good (i.e. the slope of the curve after the atoms are ejected), clearly this set of simulations does not reproduce the spreading of the width of the atomic cloud. As discussed in the main text, the measured values of T^* are indeed substantially higher than what expected from the non-interacting model. To capture the spread of the width of the distribution in real space, and so T^* , it is necessary to include the interactions in our numerical simulations. We have developed a simple ‘ad hoc’ model with the purpose of gaining a phenomenological insight on the role played by the interactions. Our model evaluates the average atom-atom scattering rate at every step, and if the value is 4 times larger than the average rate of collisions with the barriers at that time, the kinetic energy is redistributed among the three degrees of freedom. We have found that the simulations best coincide with our data if we impose that the energy is distributed 40% along x and 30% along each of the other two directions. The factor of 4 has been determined by comparing

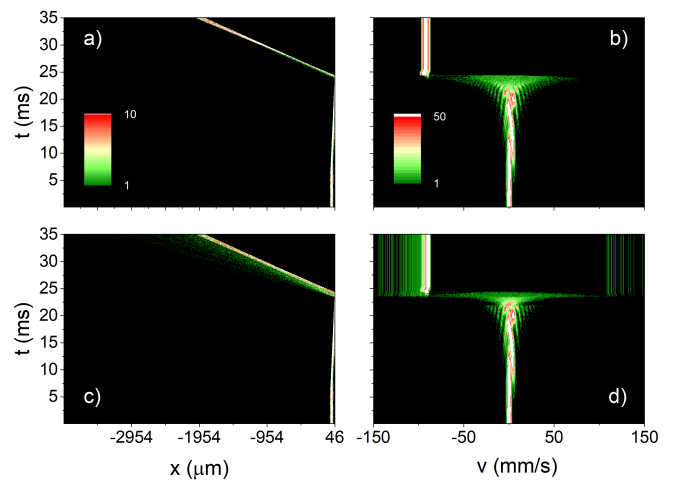


FIG. S3. (a) Time evolution of the density of the atomic cloud along the x direction according to the non-interacting numerical simulations described in the text. The contour plot is the result of stacking 350 one dimensional density profiles. (b) Same as panel (a) but in momentum space. (c) and (d) report the same time evolutions of panel (a) and (b) respectively, but for numerical simulations accounting for the interatomic interactions. In all panels the color scale has been substantially saturated to better highlight the finer details.

the results of the simulations with our data, and notably coincides with the the number of collisions needed for an atom to thermalize with an atomic thermal bath. In other words, when an atom undergoes more than 4 collisions with the other atoms while it flies from one barrier to the other, the kinetic energy that it has gained along the x direction is redistributed in all the three spatial directions. This is the case towards the end of the acceleration dynamics, where the barriers substantially compress the atomic sample (up to densities of $\simeq 10^{21} \text{ m}^{-3}$) and the average kinetic energy is boosted by the Fermi acceleration mechanism.

Since the scattering rate depends on the number of atoms, we rescale the value in the simulations to account for the actual number of atoms in the experiment, which is $\simeq 25 \times 10^3$ (note that all the other parameters and observables are independent on the number of atoms). The results of this set of simulations for the center of mass and the RMS size of the atomic cloud are the solid orange lines in Fig. S1, and are in excellent agreement with our data. The corresponding evolution of the density distribution in real and velocity space are reported in Fig. S3 c) and d). The atomic jet in real space is now more spread and has a characteristic asymmetric shape, while the evolution in momentum space is more ‘scrambled’ leading to a broader width of the distribution after the ejection. The simulations shown in Fig. 2 d) and e) are performed including the interactions, and with the same parameters as the experimental data of Fig 2c).

As an independent check, we have measured the radial

effective temperature of the atomic jet. To measure the effective temperature along the z (and y) axis, we switch off the waveguide and measure the speed at which the atomic jet expands in those directions. For the data set of Fig. S1 we measured an effective radial temperature of $15 \mu\text{K}$ (the starting temperature was 20 nK). The simulations corresponding to the orange lines in Fig. S1 deliver the exact same result. This confirms that the redistribution of the kinetic energy along the three directions due to the atomic interactions is the phenomenon behind the spreading of the width of the atomic jet.

Using our numerical simulations we can provide a conservative estimation of what can be achieved with a cold atom Fermi accelerator. With the same parameters as our experiments but without considering our technical limitations on the maximum height of the barriers achievable, and removing the interactions, we have obtained that our Fermi accelerator could produce atomic jets with $v = 1.4 \text{ m/s}$, equivalent to $E_k/k_B = 10 \text{ mK}$, with $T^* = 200 \text{ nK}$. This is only one example of acceleration compatible with typical figures that can be found in cold atoms experiments. However, we remark that we have not found any fundamental limitation to the values of v and E_k that can be obtained.

Bell's argument test

In our experiment, an atom has a certain probability $1 - P$ of being dissipated when it collides with one of the barriers. This is mainly due to the fact that the barrier potential contains also a dissipative term, that can be quantified with the light-atom scattering rate Γ_s (see above), so that $P \propto 1/\Gamma_s$. As a consequence, in a sample with N_1 atoms at the beginning of the Fermi acceleration, there will be $N_n = N_1 P^n$ atoms left after n collisions with the moving barrier. By defining the gain G so that $E_n = E_1 G^n$, where E_1 and E_n are the (kinetic) energy at the beginning and after n collisions with the moving barrier respectively, it is straightforward to show that $N_n = N_1 (E_n/E_1)^{-Q}$, with $Q = -\ln P / \ln G$. This is the celebrated Bell's result. For non-relativistic particles G and therefore Q are functions of E_n/E_1 , while for relativistic particles they are constants. Regardless, the scaling $Q \propto -\ln P$ is expected to hold for both cases.

To experimentally verify this prediction, we slightly modify the sequence of images that we send to the DMD. In particular, the moving barrier only makes a partial journey towards the fixed one. Once it collides with the atoms, accelerating them, it returns to its starting position, and repeats this motion a few times. The barrier moves at 11 mm/s , $A/k_B = 0.7 A_0/k_B \simeq 100 \mu\text{K}$, and the sequence is timed in such a way that it collides with the atoms in the center of the trap. In this way we can distinguish each collision of the atomic cloud with the moving barrier and measure the total number of atoms left in

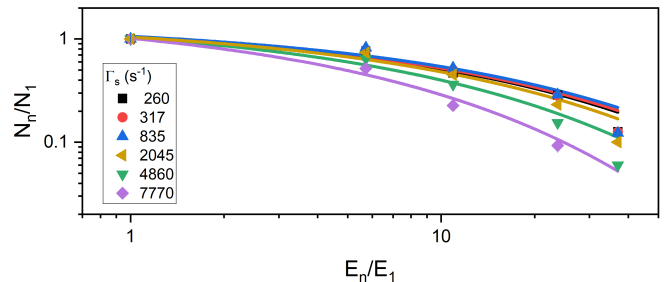


FIG. S4. Same as Fig. 4a) but with different values of Γ_s .

the accelerator after each collision. In other words, with good approximation all the atoms in the cloud undergo the same number of collisions with the moving barrier. After each collision, we measure the number of atoms utilizing the imaging along the z direction, that allows us to take absorption pictures inside the accelerator [see e.g. Fig. 2a)]. We are normally able to clearly identify 4 to 5 collisions before the spread of the atomic cloud prevents us to distinguish between different collisions. Since this imaging setup has a large magnification, the image of the cloud is heavily saturated at the starting of the sequence. For this reason, in Fig. 4 we only report the data collected after the first collision, i.e. with $n \geq 1$. Due to the same issue, for low values of Γ_s also the number of atoms after the first collision can be slightly underestimated, resulting in larger error bars. We instead measure the velocity (momentum) of the atoms by detecting how far they travel after 3 ms of time-of-flight in the waveguide, using the other imaging direction. To change Γ_s without changing the height of the barrier, we reduce the power of the laser \mathcal{P} by the same relative amount that we reduce the detuning, indeed $A \propto \mathcal{P}/\Delta$ (but $\Gamma_s \propto \mathcal{P}/\Delta^2$). The results of our measurements are shown in Fig. 4a) and Fig. S4.

With very good approximation, also confirmed by our measurements, in our system we have that $E_n = n^2 E_1$. This can be written as $E_n = E_1 G^n$, from which it follows that $G = \exp[\ln(E_n/E_1)/\sqrt{E_n/E_1}]$ and $Q = -\ln(P)/\ln(E_n/E_1) (\sqrt{E_n/E_1} - 1)$. From this it is straightforward algebra to show that $N_n = N_1 [(E_n/E_1)^{-Q}] \equiv N_1 [e^{\ln(P)(\sqrt{E_n/E_1}-1)}]$. Therefore, for our experimental implementation, the Bell's power-law actually simplifies into an exponential decay. We fit our data with the function $N_n/N_1 = (1 + B)(E_n/E_1)^{-\Theta(\sqrt{E_n/E_1}-1)/\ln(E_n/E_1)}$, where the fitting parameter B takes into account the error in the determination of N_n . From what discussed above, the Bell's argument is verified if $\Theta \equiv \ln(P)$.

Dependence of the parameters of the atomic jet on v_i and T

We have verified that, in our range of parameters ($A/k_B \gg T, mv_1^2/2k_B$), the velocity of the atomic jet is determined solely by the height of the moving barrier A and does not depend on its speed v_i . In our experiment we can change v_i either by changing the refresh rate of the DMD or by changing the number of frames in the sequence, making the motion of the barrier more or less jerky. A larger number of frames makes the motion of the barrier smoother. Our DMD was expected to reach a refresh rate of 10 kHz but we found that it cannot reliably go above 5 kHz, limiting the maximum value of v_i . As shown in Fig. S5a), as long as the speed of the barrier is lower than $\simeq 10$ mm/s, we do not observe any substantial change in the kinetic energy of the atomic jet. Because of the limitations in the refresh rate of our DMD, the Fermi accelerator becomes substantially less efficient for larger values of v_i . To reach larger velocities we need indeed to reduce the number of frames, leading to a jerky motion of the barrier. This is even more evident if we look at the E_k/T^* ratio reported in Fig. S5. When the motion of the barrier is slow but smooth, the E_k/T^* reaches its maximum value, while when the motion is fast but jerky the E_k/T^* ratio drops by a factor of $\simeq 7$. For the majority of the data reported in this work we have utilized values of v_i that enable a smooth motion of the barrier using our DMD (see caption of Fig. 3). The exceptions are the rightmost data points in Fig. 3, where we have instead utilized the highest values of v_i possible with our setup. This was done to minimize the losses of atoms from the accelerator stemming from the excessive light-atom scattering rate (see Fig. S2 and relative discussion) by minimizing the interaction time between the atoms and the barriers.

We have also measured the dependence of the parameters of the atomic jet on the initial temperature of the atomic cloud, as shown in Fig. S5c). Note that for our system the critical temperature for Bose-Einstein condensation is $\simeq 80$ nK. As expected, the velocity of the atomic jet shows no dependence on T . For what concerns the effective temperature T^* , we observe only a weak dependence. This is mostly due to the fact that the redistribution of energy driven by the atom-atom collisions described above plays a larger role in determining the speed at which the atomic jet expands. The majority of the data reported in this work are obtained with a starting T of $\simeq 20$ nK. However, for the rightmost points in Fig. 2 we have used clouds with initial temperatures of $\simeq 200$ -250 nK. This allowed us to start with more atoms and compensate for the high loss rates.

Controlling the properties of the atomic jet with the properties of the barriers

The effect of the interactions on the energy spread of the accelerated sample can be minimized by controlling the shape of the barriers. Keeping the stationary barrier unchanged, we have found that a barrier with a convex triangular shape front and a flat back is the most effective to avoid the excessive build up of density in the sample during the acceleration. As shown by the red triangles in Fig. S6a), the use of such barrier substantially reduces T^* with respect to flat barriers. We have tried several other shapes, but they seem to be less effective or ineffective in reducing T^* .

By controlling the A/A_0 ratio we can use the accelerator also as an atomic splitter, where atoms are accelerated in opposite directions along the waveguide. As reported in Fig. S6b) and S6c), the amount of atoms accelerated towards the left with velocity $|v_L| = \sqrt{2A/m}$ or towards the right with velocity $|v_R| = \sqrt{A/A_0}|v_L|$ can indeed be finely tuned with A/A_0 . Because to go right the atoms need one collision less than going left, the atomic jet going right has more atoms than the one going left when $A \simeq A_0$. Except for the data reported in Fig. 4, where $A = A_0$, all of the data reported in the main text have $A \leq 0.7A_0$, so to obtain with good approximation a single atomic jet.

Quantum Fermi acceleration

An exciting prospect is to explore the quantum version of our Fermi accelerator. In the cold atoms context, this could be done for example with a non-interacting Bose-Einstein condensate, or with single atoms trapped in the ground state of optical tweezers. As a preliminary result, here we report the results of our simulations for a generic particle in the ground state of a one dimensional harmonic oscillator with frequency 40 Hz. We numerically simulate this system with split-step methods on a grid of 8192 sites and total length 100 μm . The time step used is 100 ns and the total duration is 26 ms. The evolution of the density distribution in real and momentum space for an accelerator with the same parameters as in our experiment is reported in Fig. S7. The quantum Fermi accelerator works very similarly to the classical version studied in this work, being able to accelerate a wavepacket without any noticeable increase in its width in momentum space. The peculiar dynamics in momentum space is apparent also in the quantum version.

We have preliminarily explored the potential of a quantum Fermi accelerator as a coherent splitter. To this end we have used a grid of 8192 sites and total length 300 μm and a harmonic oscillator with frequency 100 Hz. The time step used is 100 ns and the total duration is 9 ms. The results for different values of A/A_0 are reported

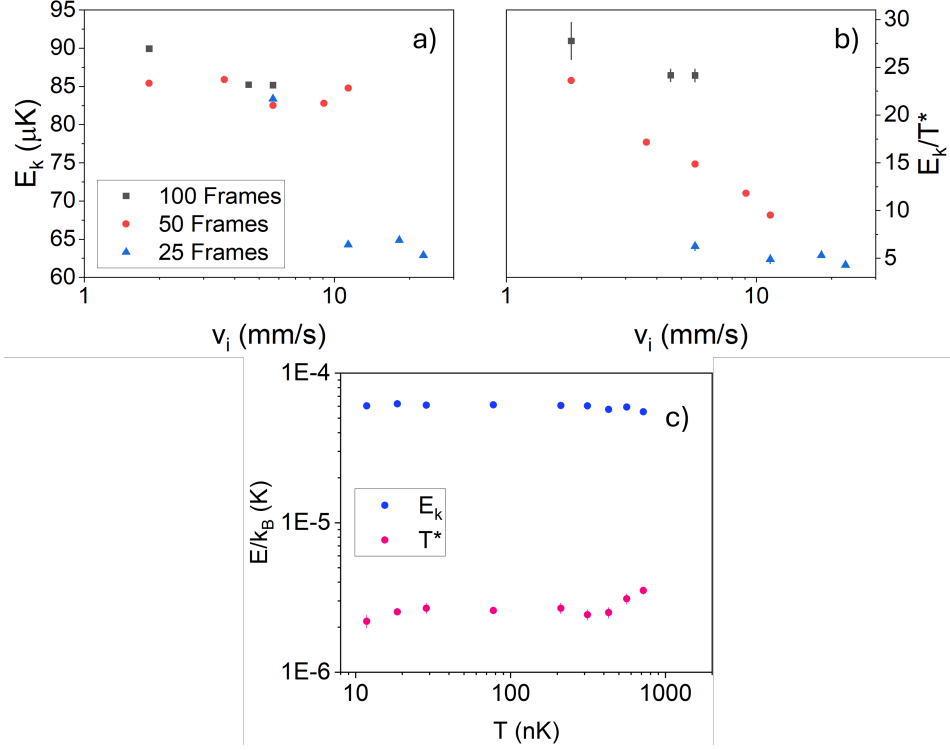


FIG. S5. (a) Kinetic energy of the atomic jet as a function of the velocity of the moving barrier, for different number of frames. (b) Same as (a) but for the ratio between the kinetic energy and the effective temperature of the atomic jet. The errorbars are 1σ statistical errors. (c) Kinetic energy (blue points) and effective temperature (red points) as a function of the initial temperature of the atomic cloud. The errorbars are 1σ statistical errors.

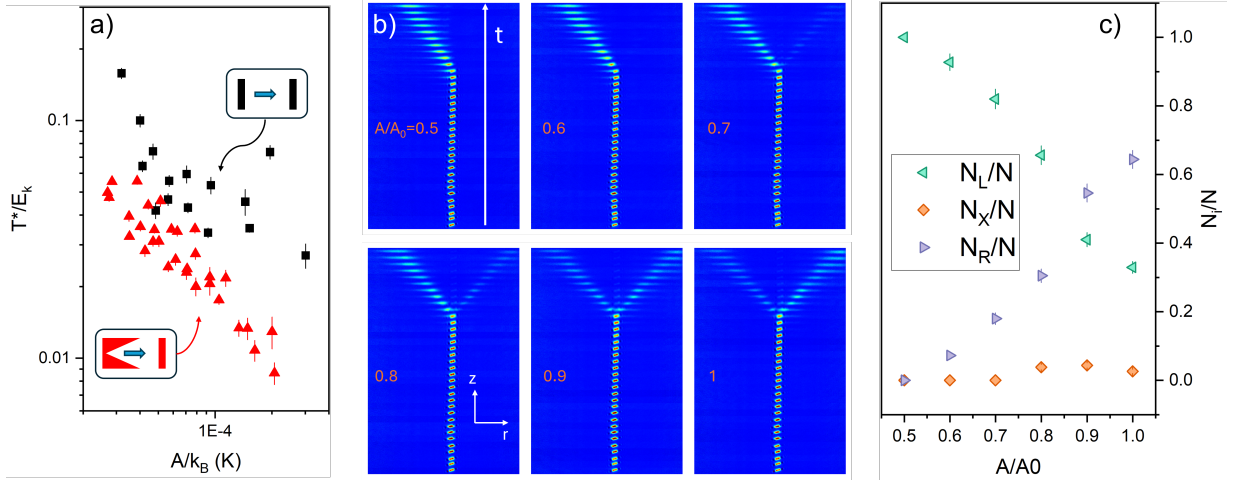


FIG. S6. (a) Ratio between the effective temperature of the accelerated cloud T^* and its average kinetic energy E_k as a function of the amplitude of the moving barrier A . Black square symbols are for a flat moving barrier (as sketched in the inset), while red triangle symbols are for a convex triangular moving barrier (sketched in the inset). For all data points $v_i = 4.4$ mm/s , $T = 20$ nK and $A/A_0 = 0.7$. The errorbars are given by the error of the fit done to determine T^* . (b) Stacked in situ absorption images with the same dimensions and parameters as Fig. 2b) except that for the A/A_0 ratio that here is varied across the panels to control the splitting of the atomic cloud, as indicated. (c) Number of atoms going left (N_L), right (N_R) or remaining in the accelerator (N_X) normalized by the total atom number N as a function of A/A_0 for the data in panel (b). The errorbars come from the fit to the atomic cloud with a Gaussian profile.

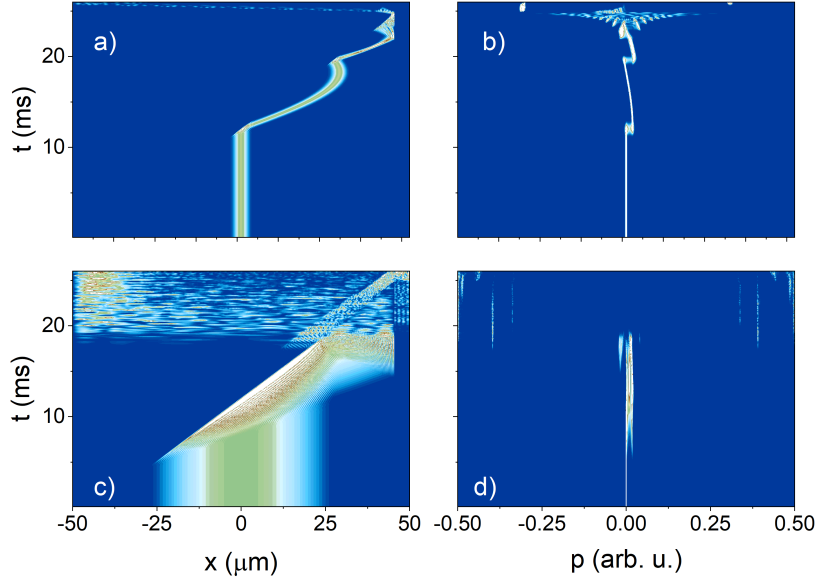


FIG. S7. (a) Numerically simulated time evolution of the probability density distribution of a one dimensional Gaussian wavepacket that is accelerated by a Fermi accelerator like the one used in this work. The contour plot results from the stacking of 260 one dimensional probability density profiles. (b) The same as (a) but in momentum space. The color scale has been saturated to highlight the finer features. (c) and (d) are the same as (a) and (b) respectively, but for an (effectively) one dimensional Bose-Einstein condensate (see text).

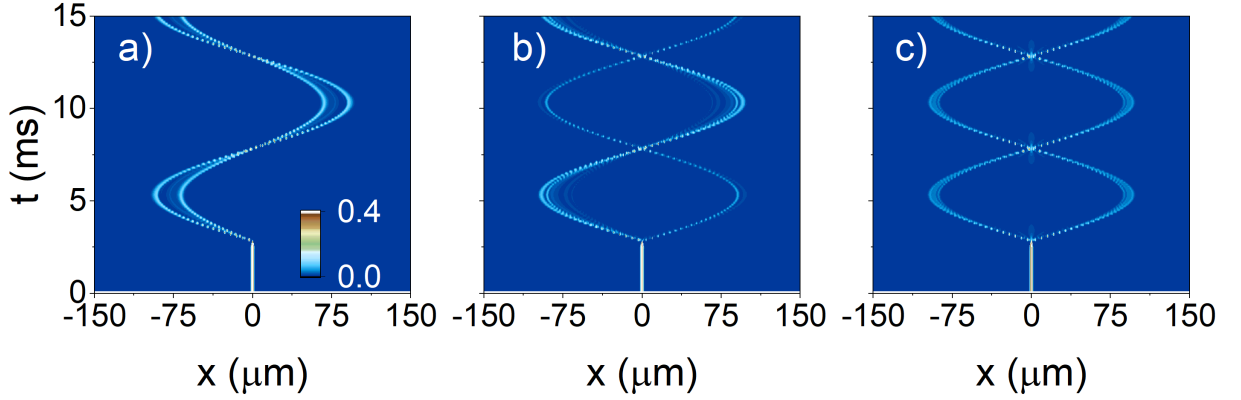


FIG. S8. Numerically simulated time evolution of the probability density distribution of a one dimensional Gaussian wavepacket that is split by two barriers converging towards $x = 0$ with same but opposite velocity. (a) is for the barrier with positive velocity having half the height of the other one, (b) is for a 0.9 ratio, while (c) is for two identical barriers. The color scale is saturated to highlight the finer features.

in Fig. S8. In this case two moving barriers are approaching the center of the trap with equal but opposite velocities. As for our data in Fig. 3, by changing A/A_0 it is possible to control the splitting of the wavefunction. We observe that the splitting actually manifests as an interference pattern that oscillates in space with a period given by the harmonic trap, suggesting that the quantum Fermi accelerator could in principle be used as a coherent splitter.

We also investigated the effect of the Fermi accelerator on a Bose-Einstein condensate. To do so we have evolved the non-polynomial Schrödinger equation (NPSE), which

is an effective one dimensional non-linear Schrödinger equation, using split-step methods on a grid of 8192 points and total length 100μ , with a time step of 100 ns for a total duration of 26 ms. We have used 2×10^4 ^{87}Rb atoms in the same trapping potential as the one described earlier. As shown in Fig. S3, our simulations show that an interacting Bose-Einstein condensate cannot be actually accelerated, but gets instead destroyed during the acceleration process. This is expected because the barrier moves faster than the speed of sound in the condensate, and is in line with what observed in the experiment. Indeed as described earlier, even if we start

in most cases from a cloud with substantial condensed fraction, already after the first collision with the barrier we do not detect any remaining condensate.